Optical properties of fluid hydrogen at the transition to a conducting state

in press at Physical Review Letters

TITLE

Optical properties of fluid hydrogen at the transition to a conducting state

AUTHORS

R. Stewart McWilliams,[1,2,3*] D. Allen Dalton,[1] Mohammad F. Mahmood,[1,3] Alexander F. Goncharov[4,1,5*]

AFFILATIONS

[1] Geophysical Laboratory, Carnegie Institution of Washington, 5251 Broad Branch Road NW, Washington DC, 20015, USA

[2] School of Physics and Astronomy and Centre for Science at Extreme Conditions, University of Edinburgh, Peter Guthrie Tait Road, Edinburgh, UK EH9 3FD

[3] Dept. of Mathematics, Howard University, 2400 Sixth Street NW, Washington DC, 20059, USA

[4] Key Laboratory of Materials Physics, Institute of Solid State Physics, Chinese Academy of Sciences, 350 Shushanghu Road, Hefei, Anhui 230031, China

[5] University of Science and Technology of China, Hefei, Anhui 230026, China

[*]Corresponding authors

SECTION: L7

PACS: 62.50.-p, 81.30.Dz, 78.40.-q, 07.35.+k

ABSTRACT

We use fast transient transmission and emission spectroscopies in the pulse laser heated diamond anvil cell to probe the energy-dependent optical properties of hydrogen at pressures of 10-150 GPa and temperatures up to 6000 K. Hydrogen is absorptive at visible to near-infrared wavelengths above a threshold temperature that decreases from 3000 K at 18 GPa to 1700 K at 110 GPa. Transmission spectra at 2400 K and 141 GPa indicate that the absorptive hydrogen is semiconducting or semi-metallic in character, definitively ruling out a first-order insulator-metal transition in the studied pressure range.

TEXT

Realizing metallic hydrogen and understanding its properties is fundamental for achieving predicted high temperature superconductivity [1], exploring the regime of inertial confinement fusion [2], and resolving the structure and dynamics of giant planetary interiors [3-7]. The metallic state has not been reached yet in the solid at pressures as high as 360 GPa [8-10], but experiments [3,11-16] and theoretical calculations [5,16-27] probing the fluid state at high temperature document an insulator-metal transition (IMT). This fluid metallic state has been theorized to be even the ground state at sufficiently high pressures [19,20], however recent experiments suggest more complex behavior [16,28].

While the underlying physics of metallization in hydrogen is thought to be related to a Mott-like mechanism (band overlap), the essential parts of this phenomenon remain uncaptured because of difficulties in finding appropriate theoretical approximation methods [25-27] and experimental challenges. With increasing pressure, the fluid IMT is expected to exhibit a *critical point* where it transitions from being continuous to discontinuous (first-order), and merge with

46 the melting line in the limit of high densities [19,20]. Different theoretical studies agree about the
47 transition character, but the location of the critical point varies substantially, with modern
48 estimates ranging as low as 90 GPa [4,5,19,21,22,25-27].

49 Experiments on fluid hydrogen using shock compression measured gradual increases in
50 electrical conductivity and optical reflectivity to constant, metallic values with increasing
51 temperature and pressure up to 90 GPa [11,13,14], evincing a continuous IMT below this
52 pressure. Between 90 and 140 GPa shock experiments were conducted without direct
53 temperature measurements, leaving the gradual increase and saturation of conductivity detected
54 in this region [3,12,29] open to interpretation: the data are consistent with a continuous IMT
55 [3,12,29] but also show characteristics of a first order IMT naturally broadened by adiabatic
56 compression (e.g. Ref. [30]). Recent isentropic compression measurements suggest the IMT
57 becomes first order by 285 GPa [16], but also assumed temperature, leaving a broad pressure
58 range [3,12,16,29] where the nature of the IMT remains poorly characterized. Static
59 compression, diamond anvil cell (DAC) experiments showed that direct temperature
60 measurements are possible in the metallization regime at high pressure, and detected a fluid
61 phase transition at ~120 GPa, though were not able to provide any characteristics of the
62 transformed state [15].

63 Hydrogen is a highly reactive and diffusive material, so is challenging to contain in high
64 temperature and pressure experiments for long periods [28,31]. Dynamic compression has
65 probed hydrogen beyond several thousand K at high pressures on microsecond or faster
66 timescales [3,11-14,29], whereas DAC experiments limited to longer timescales reached 1000
67 and 1800 K using resistive [28] and laser heating [15,31,32], respectively.

In this Letter we describe microsecond, single-pulse laser heating DAC experiments on hydrogen that reach novel conditions not previously characterized by dynamic or static studies (Fig. 1). Time-resolved optical emission and transmission spectroscopy determines sample temperature T and corresponding optical absorptivity α during heat cycles [33,34]. A 4-10 μs long laser pulse heats a metallic (Ir) foil in a hydrogen sample, and heat propagates across the adjacent hydrogen creating a localized heated excited state of several μm in linear dimensions and a few μs long. Transient absorption probing using a continuous laser (CW: 532 nm) and pulsed broadband supercontinuum (BB: 1 MHz, 150 ps, 400-900 nm) was performed by transmission through a hole in the foil at the heated region. Fits of emission spectra to a Planck distribution determined temperature with a time resolution of 0.5-5 μs.

To ensure our measurements probed pristine hydrogen, several precautions were taken. Pressure was measured before and after the heat cycles using Raman spectra of the hydrogen vibron [35] and diamond edge [36], and ruby fluorescence [37]. Vibron signal from the heated area was confirmed before and after heating [34]. Continued heating resulted in decreasing vibron signal, pressure changes (usually but not always negative), decreasing foil hole diameters [34], and occasional anvil fracturing, evincing rapid hydrogen diffusion and loss. Complete loss occurred within ~1 ms of total heating time. Weak Raman lines attributed to Ir hydride [38] appeared in one sample subjected to prolonged heating at high temperature [34], but not in reported experiments.

Upon increasing laser power, time histories of thermal emission during heat cycles exhibited a drastic shift in behavior, similar to that seen in noble gases as a consequence of high-temperature absorption onset [33]. For low peak laser power, the temperature followed the laser power history (Fig. 2a), having a distinct initial peak. With increasing power, there was a

transition to a different thermal response, where temperature did not follow laser power, but instead rose and remained roughly constant, forming a plateau that persisted for an especially long duration (Fig. 3). To examine this transition we performed finite element (FE) models [33,34,39] to investigate how properties of hydrogen samples, such as a temperature-dependent absorption, control temperature history. The lower-temperature behavior is expected for a transparent sample, i.e. where the laser is absorbed entirely in the foil surface. The higher-temperature behavior could not be explained if the sample remained transparent; instead an abrupt increase in sample absorption with temperature (to $\alpha \approx 0.1$ to 1 μm^{-1}) is needed to reproduce the long temperature plateau, which occurs near the temperature of transition to the absorptive state. In this regime, hydrogen is heated directly by bulk absorption of laser energy, and this delocalization of heat energy compared to absorption at the foil surface limits the achievable temperature, producing the plateau effect.

Transient absorption measurements (Fig. 2) confirm the change in thermal history is correlated with increased optical absorption. Here, absorption coefficient $\alpha = -\ln(I_H/I_C)/d$, where d is the thickness of the hot region (estimated from FE calculations, and of order 1 μm at 141 GPa), while I_C and I_H are transmitted probe intensities through cold and hot samples, respectively. Peak α near 1 μm^{-1} are consistently inferred, with total uncertainty of about an order of magnitude largely due to thickness uncertainty and reproducibility.

To compare our optical measurements in a wide, previously unexplored region of the phase diagram to prior data, we interpolated direct-current (DC) conductivity (σ_0) measurements on fluid hydrogen [3,11,12,29,40] using an experimentally-consistent model [34] having the form $\sigma^* = \sigma_m^* - \sigma_j^*\{1 - 0.5\,\mathrm{erfc}[(T^* - T_c^*)/T_w^*]\}$, where $\sigma^* = \log(\sigma_0)$ and $T^* = 1/T$. This model has a sigmoidal temperature dependence that reproduces the Arrhenius- or semiconductor-

like proportionality of $\sigma^* \propto T^*$ during the IMT [11,12,29], with constant conductivity in purely metallic (σ_m^*) [13,14,29] and insulating ($\sigma_m^* - \sigma_j^*$) [40] states; the transition temperature (T_c^*) and width (T_w^*) were taken to vary linearly with density [34].

Absorption spectra at 141 GPa and 2,400 K show increasing absorption with photon energy across the visible (Fig. 4a). Semiconductor-like absorption is one possible explanation: electronic band gaps on the order of the present optical energies have been reported in dense hydrogen [3,8,9,12,16,29,41,42]. The data do not permit the exact assignment to existing semiconductor or semi-metal models. However, given the disordered nature of the material and rather large values of the absorption coefficients (up to ~10^6 m^{-1}), we suggest that observed absorption is due to optical processes between extended states, which are well described by Tauc's relation $\alpha = A(\hbar\omega - E_g)^2/\hbar\omega$. This well fits the data, implying a gap E_g of 0.9±0.3 eV. In this semiconductor picture, hydrogen is electrically conductive due to thermal excitation of electrons. Assuming an effective carrier mass of 0.5-1 m_e [13,33] the DC conductivity at these conditions is predicted to be 5-23 S/cm for E_g=0.9 eV, in agreement with that determined from shock data (~15 S/cm) [43]. The spectral character is consistent with theory for semiconducting hydrogen at similar pressure and lower temperature [16] which may be similarly described by the Tauc model.

Conductivity at optical frequencies is $\sigma = n\alpha c\varepsilon_0$, where n is the real index of refraction [44,45] which is weakly dependent on material properties, and always of order 10^0 [34]. Thus, σ is determined principally by α, which varies by many orders of magnitude during electronic transformation. The conductivity at 2400 K and 141 GPa varies between ~70 and ~220 S/cm from 1.55 to 2.3 eV, and this extrapolated to zero energy is consistent with the DC conductivity

of ~15 S/cm (Fig. 4b). The decrease in conductivity with energy is inconsistent with the simple Drude model of free carriers widely used for hydrogen at extreme conditions [2,11-14,16,17].

A modified Drude model, after Smith [46], given by $\sigma = \sigma_0[1 + C\ (1 - \omega^2\tau^2)/(1 + \omega^2\tau^2)]/[(1 + C)(1 + \omega^2\tau^2)]$ and incorporating reduced electron mobility through a backscattering term *C*, does provide an adequate representation of the data including the DC limit (Fig. 4b). This model has features typically observed in poor metals at the boundary of metallization transitions such as mercury [46] and argon [33], suggesting its applicability for hydrogen at the IMT. The parameter *C*, a measure of how closely the spectrum follows the Drude (free-electron) approximation, ranges from 0 to -1, with $C = 0$ (minimum backscattering) corresponding to the Drude form. Fits to our data show *C* is closer to -1 at conditions of incipient metallization (Fig. 4c). This is consistent with theories for conducting hydrogen [17,21,23,24], which are well described by a Smith-Drude model with $C \neq 0$ [34]. Scattering times τ from Smith-Drude fits are insensitive to pressure and temperature (Fig. 4d) despite conditions sampled by experiment and theory ranging from 24-6,000 GPa, 1,000-125,000 K, and 0.3-5.4 g/cc in pressure, temperature, and density, respectively [17,21,23,24], and are consistent with the expected minimum scattering time (Ioffe-Regal limit) [12,13] where scattering occurs at the interatomic spacing. Conductivity peaks at $\omega_m \approx 1/\tau$ when $C \approx -1$, or $\hbar\omega_m \approx 10$ eV for the present data. The fact that conduction is maximized in conjunction with the shortest-distance carrier motion possible indicates that transport is dominated by motion of bound carriers, such as hopping [18], as opposed to unimpeded long-distance flow.

The temperature at which absorbing hydrogen appears (at detection limit $\alpha \approx 0.1$ μm^{-1}) decreases weakly with pressure, remaining at 1700-2500 K at 30-110 GPa (Fig. 1). Here $\sigma_0 \approx 10^{-3}$ S/cm, which is below the optical conductivity, $\sigma \approx 10^0$ S/cm. The data at 141 GPa

and 2400 K have $\sigma_0 \sim 10^1$ S/cm, and $\sigma \sim 10^2$ S/cm at visible frequencies (Fig. 4b). Fluid hydrogen thus shows optical properties characteristic of a weak metal [17,21,23,24] and a semiconductor undergoing gap closure [16] (σ increasing with frequency) throughout the observed pressure range at temperatures of 1700-2500 K. Measured optical conductivities (Fig. 4) are less than those of the metallic state (~2000 S/cm) [12,29], whereas optical reflectivity *R*, estimated by assessing the Fresnel reflectivity between insulating (cold) and optically transformed (hot) states in the experiment, is $R \sim [(4n\omega/\alpha c)^2 + 1]^{-1}$ or less than ~1% at presently examined conditions.

Our data directly show hot fluid hydrogen retains a significant band gap to above 140 GPa pressure (Fig. 4) and temperatures of 2000-3000 K. Prior interpretations of conductivity data, assuming a density-dependent, temperature-independent gap, predicted metallization at these conditions (densities above 0.32 mol-H_2/cc) via compressive gap closure [3,12,29]. The difference between our direct measurement and the prior model result is attributed to temperature dependence of the gap. Indeed, the temperature at which absorption appears in fluid hydrogen is nearly density- and pressure-independent between 30 – 110 GPa, suggesting gap closure is primarily thermal rather than compressive.

Our definitive observation of a weakly conducting, semiconductor-like state of hot fluid hydrogen in measurements to 150 GPa rules out the possibility of a rapid or first-order transformation between insulator and metal at these pressures. This is inconsistent with some *ab-initio* theoretical predictions [5,19,21,22] and supports more recent theories employing nonlocal density functionals and nuclear quantum effects [25] or quantum Monte Carlo molecular dynamics [27], which place a critical point at 250-375 GPa. Isentropic compression measurements find the IMT becomes first order by 285 GPa [16], suggesting together with our

results an experimental critical point between 150 and 285 GPa. Also, the gap in temperature between insulating and metallic conditions appears to be decreasing with pressure in the studied range, consistent with the transition sharpening towards a critical point at higher pressures (Fig. 1): at 22 GPa, reflectivity [14] onsets 3710 K above absorption; at 45 GPa, the difference is 1540 K). Parallel behavior is seen in the DC conductivity (Fig. 1).

Prevailing first-principles models for hydrogen and hydrogen-bearing systems at high pressure and temperature in giant planets [4,5,47] thus require a significant reassessment. Compared with these theories, metallic conditions occur at higher pressure and temperature (i.e. deeper within the planets), potentially influencing atmospheric coupling with the metallic layer [6,7] and the conditions of hydrogen-helium phase separation. For example, as conditions of phase separation are correlated with the location of the critical point [4,5,47], the increased pressure of the critical point required by our direct observations to 150 GPa suggests phase separation is unlikely to have occurred in Jupiter [34].

Our optical properties measurements on hydrogen cover a wide, previously unexplored region of the phase diagram and bridge large gaps between prior dynamic and static compression measurements of transformation and transport properties. Our data show the presence of an intermediate absorptive but not metallic state of hydrogen at the boundary between insulating and metallic regimes in a wide pressure range (10-150 GPa). This is inconsistent with first-order insulator-metal transition and compression-driven gap closure that were previously inferred in this region from experiments and theory.

We thank S. Lobanov and M. Ahart for experimental assistance, C.T. Seagle, R. Boehler, and R.J. Hemley for helpful discussions, and R.T. Howie, V. Struzhkin, E. Gregoryanz, and three anonymous reviewers for constructive suggestions on this manuscript. This work was supported

by the NSF Major Research Instrumentation program, NSF EAR-1015239, NSF EAR-1520648 and NSF EAR/IF-1128867, the Army Research Office (56122-CH-H), the Carnegie Institution of Washington, the Deep Carbon Observatory Instrumentation grant, the British Council Researcher Links programme, the DOE NNSA Carnegie/DOE Alliance Center (DE-FC52-08NA28554), the DOE EFRC for Energy Frontier Research in Extreme Environments (EFREE), and NSFC (No. 21473211).

FIGURE CAPTIONS

FIG. 1. (color) Phase diagram of hydrogen. Black lines are phase boundaries. Present measurements are filled circles for transparent (white), and absorbing (grey, black) hydrogen; black points are characterized via direct transient absorption measurement (Fig. 2) whereas grey points correspond to anomalous temperature responses observed upon increasing heating laser power (Fig. 3). A thermal pressure of 2.5 GPa/1000 K [48] is included. The heavy black line is onset of absorbing hydrogen in the present data. Prior measurements are the onset of reflectivity in shock compression [14] (crosses and dotted line), the onset of visible absorption in isentropic compression [16] (squares and dashed line), the location of anomalies in temperature with increasing heating laser power in the DAC [15] (stars), and the DC conductivity (color map) based on interpolated data [3,11,12,29,34,40]. The melting curve is taken from Ref. [28] and the metallization line is the saturation of DC conductivity. White lines are interior conditions of Jupiter [49] and Saturn [50].

FIG. 2. (color) Transient absorption and emission measurements in hydrogen at 141 GPa. (a) Laser power (upper panel) and spectrogram showing transient absorption (lower panel). (b) Time histories of absorption at different wavelengths using pulse referencing [33,34]. (c) Transmission spectrum averaged over 2 to 5 μs where absorption (and temperature) is roughly constant. (d) Emission spectrogram (20 spectrograms stacked), with inset showing gray-body Planck fit to data at 2 to 5 μs. Temperature in this time interval was 2400(300) in a series of heat cycles at this laser power.

FIG. 3. (color) Temperature histories at 30 GPa with finite element model predictions. Two measurements (open symbols: vertical bars are temperature uncertainty, horizontal bars are time resolution) are presented with finite element models [33,34,39] with and without an onset of infrared absorption in hydrogen at a critical temperature of ~3300 K (solid and dashed lines, respectively). Below the critical temperature (blue points), models (grey) are indistinguishable and follow behavior typical for a transparent sample with laser energy absorption on the foil surface [39]. For experiments achieving the critical temperature (red points), models (black) show the result of sample absorption: rather than an initial peak and decay that scaled with laser power, temperature is limited to values near the critical temperature [33]. Laser power increased from 65 to 155 W between the models. Above 100 GPa transient absorption occurred without this effect, since thinner samples at high pressure did not become infrared-optically thick when heated.

FIG. 4. Optical properties of hydrogen. Data at 141 GPa and 2400(300) K are open circles (error bars are systematic), theoretical predictions are crosses, and fits are lines. (a) Absorption spectra with Tauc fits, with theory for semiconducting states at 1600-1700 K, 101-159 GPa [16]. (b) Conductivity spectra with Smith-Drude fits. The DC conductivity corresponding to the present data and used in the fitting is $\sigma_0 = 15$ S/cm (triangle). Theory for metal and nonmetal states are for 1000 K, 170 GPa [21]. (c) Smith-Drude backscattering parameter *C* and (d) scattering time τ are from theory [17,21,23,24,34] and experiment; shaded region in (c) is the conditions for metallization [12,21,29] and in (d) the calculated minimum scattering time (Ioffe-Regal limit) [12,13] for relevant conditions.

257

FIGURES

FIG. 1

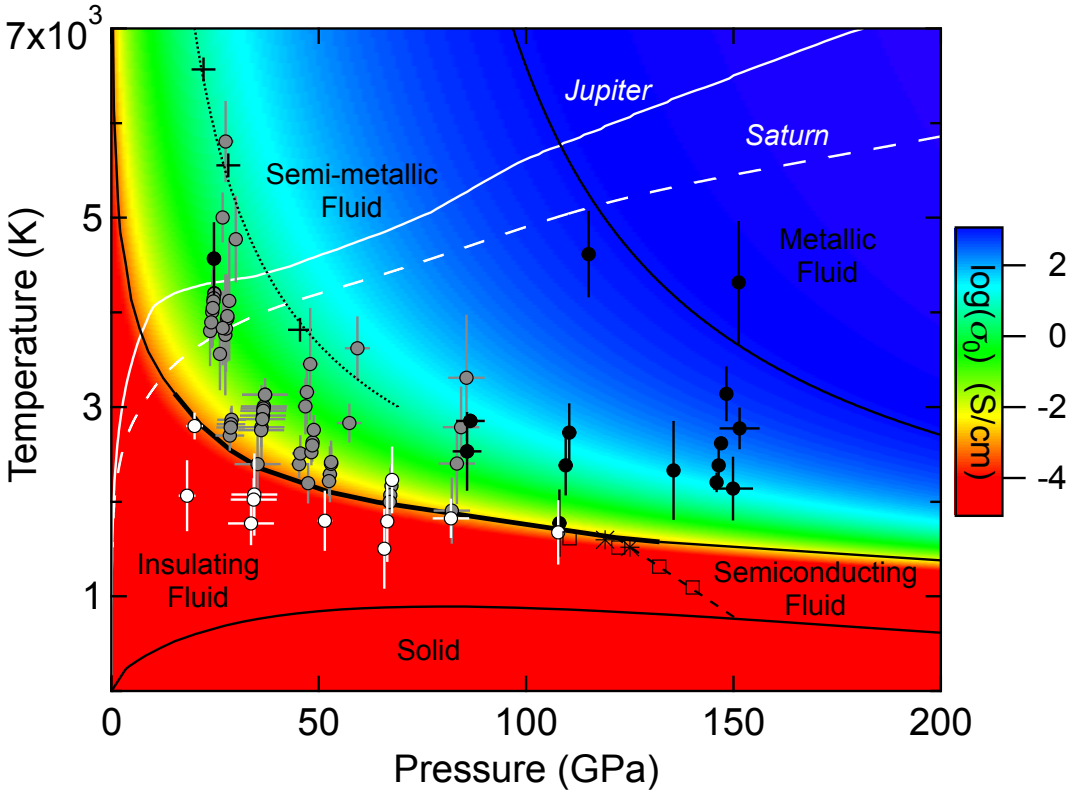

FIG. 2

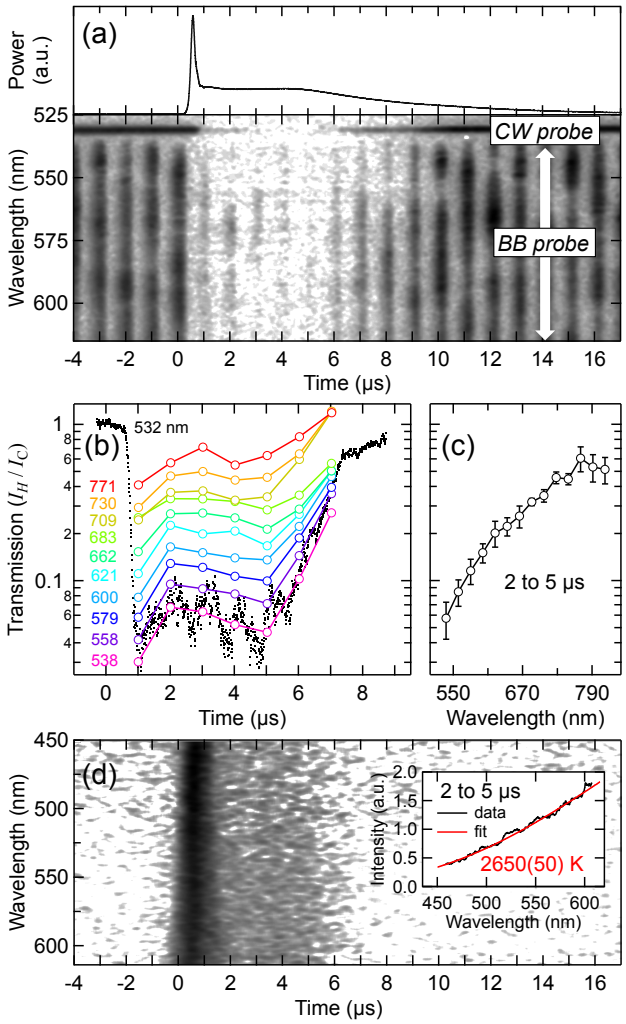
(a)
Power (a.u.)
525
550
575
600
Wavelength (nm)
CW probe
BB probe
-4 -2 0 2 4 6 8 10 12 14 16
Time (μs)
(b)
532 nm
771
730
709
683
662
621
600
579
558
538
Transmission (I_H / I_C)
1
0.1
0 2 4 6 8
Time (μs)
(c)
2 to 5 μs
550 670 790
Wavelength (nm)
(d)
Wavelength (nm)
450
500
550
600
-4 -2 0 2 4 6 8 10 12 14 16
Time (μs)
Intensity (a.u.)
2 to 5 μs
data
fit
2650(50) K
0.0 0.5 1.0 1.5 2.0
450 500 550 600
Wavelength (nm)

FIG. 3

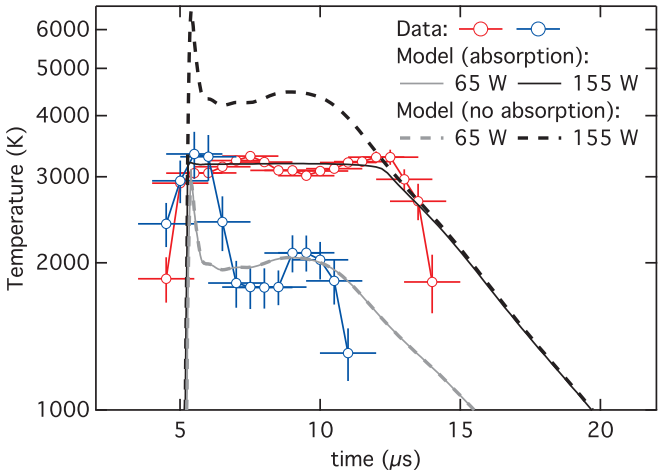
Data:
Model (absorption):
65 W
155 W
Model (no absorption):
65 W
155 W
Temperature (K)
6000
5000
4000
3000
2000
1000
5
10
15
20
time (μs)

FIG. 4

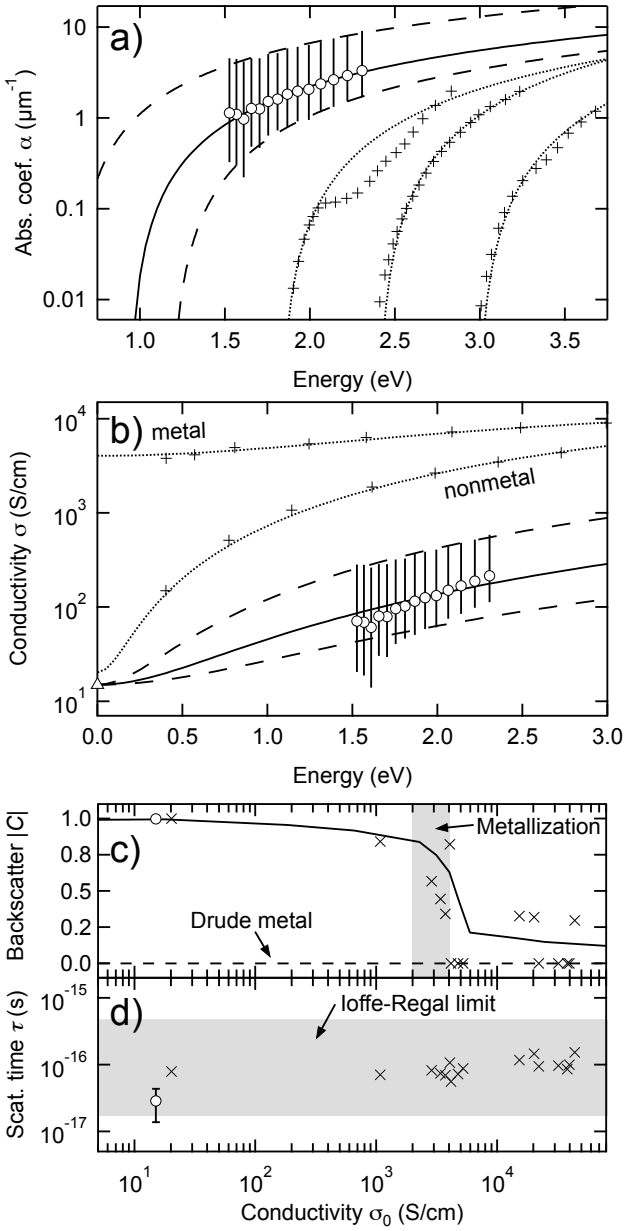
a)
Abs. coef. α (μm⁻¹)
Energy (eV)
b) metal
nonmetal
Conductivity σ (S/cm)
Energy (eV)
c)
Backscatter |C|
Metallization
Drude metal
d)
Scat. time τ (s)
Ioffe-Regal limit
Conductivity σ0 (S/cm)

REFERENCES

[1] N. W. Ashcroft, Physical Review Letters **21**, 1748 (1968).
[2] S. X. Hu, L. A. Collins, V. N. Goncharov, T. R. Boehly, R. Epstein, R. L. McCrory, and S. Skupsky, Physical Review E **90**, 033111 (2014).
[3] W. J. Nellis, S. T. Weir, and A. C. Mitchell, Science **273**, 936 (1996).
[4] W. Lorenzen, B. Holst, and R. Redmer, Physical Review Letters **102** (2009).
[5] W. Lorenzen, B. Holst, and R. Redmer, Physical Review B **84**, 7, 235109 (2011).
[6] M. Heimpel and N. Gómez Pérez, Geophysical Research Letters **38** (2011).
[7] T. Gastine, J. Wicht, L. D. V. Duarte, M. Heimpel, and A. Becker, Geophysical Research Letters **41**, 5410 (2014).
[8] P. Loubeyre, F. Occelli, and R. LeToullec, Nature **416**, 613 (2002).
[9] R. T. Howie, C. L. Guillaume, T. Scheler, A. F. Goncharov, and E. Gregoryanz, Physical Review Letters **108**, 125501 (2012).
[10] C.-s. Zha, Z. Liu, M. Ahart, R. Boehler, and R. J. Hemley, Physical Review Letters **110**, 217402 (2013).
[11] W. J. Nellis, A. C. Mitchell, P. C. McCandless, D. J. Erskine, and S. T. Weir, Physical Review Letters **68**, 2937 (1992).
[12] W. J. Nellis, S. T. Weir, and A. C. Mitchell, Physical Review B **59**, 3434 (1999).
[13] P. M. Celliers, G. W. Collins, L. B. Da Silva, D. M. Gold, R. Cauble, R. J. Wallace, M. E. Foord, and B. A. Hammel, Physical Review Letters **84**, 5564 (2000).
[14] P. Loubeyre, S. Brygoo, J. Eggert, P. M. Celliers, D. K. Spaulding, J. R. Rygg, T. R. Boehly, G. W. Collins, and R. Jeanloz, Physical Review B **86**, 9, 144115 (2012).
[15] V. Dzyabura, M. Zaghoo, and I. F. Silvera, Proc. Natl. Acad. Sci. U. S. A. **110**, 8040 (2013).
[16] M. D. Knudson, M. P. Desjarlais, A. Becker, R. W. Lemke, K. R. Cochrane, M. E. Savage, D. E. Bliss, T. R. Mattsson, and R. Redmer, Science **348**, 1455 (2015).
[17] L. A. Collins, S. R. Bickham, J. D. Kress, S. Mazevet, T. J. Lenosky, N. J. Troullier, and W. Windl, Physical Review B **63**, 11, 184110 (2001).
[18] R. Redmer, G. Röpke, S. Kuhlbrodt, and H. Reinholz, Physical Review B **63**, 233104 (2001).
[19] S. Scandolo, Proceedings of the National Academy of Sciences **100**, 3051 (2003).
[20] S. A. Bonev, E. Schwegler, T. Ogitsu, and G. Galli, Nature **431**, 669 (2004).
[21] M. A. Morales, C. Pierleoni, E. Schwegler, and D. M. Ceperley, Proc. Natl. Acad. Sci. U. S. A. **107**, 12799 (2010).
[22] I. Tamblyn and S. A. Bonev, Physical Review Letters **104**, 4 (2010).
[23] S. Hamel, M. A. Morales, and E. Schwegler, Physical Review B **84**, 165110 (2011).
[24] L. A. Collins, J. D. Kress, and D. E. Hanson, Physical Review B **85**, 233101 (2012).
[25] M. A. Morales, J. M. McMahon, C. Pierleoni, and D. M. Ceperley, Physical Review Letters **110**, 065702 (2013).
[26] G. Mazzola, S. Yunoki, and S. Sorella, Nat Commun **5** (2014).
[27] G. Mazzola and S. Sorella, Physical Review Letters **114**, 105701 (2015).
[28] R. T. Howie, P. Dalladay-Simpson, and E. Gregoryanz, Nat Mater **14**, 495 (2015).
[29] S. T. Weir, A. C. Mitchell, and W. J. Nellis, Physical Review Letters **76**, 1860 (1996).

[30] J. H. Eggert, D. G. Hicks, P. M. Celliers, D. K. Bradley, R. S. McWilliams, R. Jeanloz, J. E. Miller, T. R. Boehly, and G. W. Collins, Nature Physics **6**, 40 (2010).
[31] N. Subramanian, A. F. Goncharov, V. V. Struzhkin, M. Somayazulu, and R. J. Hemley, Proc. Natl. Acad. Sci. U. S. A. **108**, 6014 (2011).
[32] A. F. Goncharov and J. C. Crowhurst, Physical Review Letters **96**, 4, 055504 (2006).
[33] R. S. McWilliams, D. A. Dalton, Z. Konopkova, M. F. Mahmood, and A. F. Goncharov, Proceedings of the National Academy of Sciences **112**, 7925 (2015).
[34] *See Supplemental Material at [URL will be inserted by publisher] for supporting figures and data.*
[35] H. K. Mao and R. J. Hemley, Reviews of Modern Physics **66**, 671 (1994).
[36] Y. Akahama and H. Kawamura, High Pressure Research **27**, 473 (2007).
[37] H. K. Mao, J. Xu, and P. M. Bell, Journal of Geophysical Research-Solid Earth and Planets **91**, 4673 (1986).
[38] T. Scheler, M. Marques, Z. Konopkova, C. L. Guillaume, R. T. Howie, and E. Gregoryanz, Physical Review Letters **111**, 5, 215503 (2013).
[39] J. A. Montoya and A. F. Goncharov, J. Appl. Phys. **111**, 9 (2012).
[40] W. L. Willis, Cryogenics **6**, 279 (1966).
[41] C.-S. Zha, Z. Liu, and R. J. Hemley, Physical Review Letters **108**, 146402 (2012).
[42] A. F. Goncharov, J. S. Tse, H. Wang, J. Yang, V. V. Struzhkin, R. T. Howie, and E. Gregoryanz, Physical Review B **87**, 024101 (2013).
[43] DC conductivity is taken from the lower end of the temperature range achieved at this laser power, since the stacked transient absorption data (Fig. 2) is dominated by those cycles reaching lower temperature and lower absorption.
[44] W. J. Evans and I. F. Silvera, Physical Review B **57**, 14105 (1998).
[45] R. J. Hemley, M. Hanfland, and H. K. Mao, Nature **350**, 488 (1991).
[46] N. V. Smith, Physical Review B **64**, 155106 (2001).
[47] M. A. Morales, S. Hamel, K. Caspersen, and E. Schwegler, Physical Review B **87**, 4, 174105 (2013).
[48] A. F. Goncharov, J. C. Crowhurst, J. K. Dewhurst, S. Sharma, C. Sanloup, E. Gregoryanz, N. Guignot, and M. Mezouar, Physical Review B **75**, 224114 (2007).
[49] N. Nettelmann, A. Becker, B. Holst, and R. Redmer, Astrophys. J. **750**, 10, 52 (2012).
[50] N. Nettelmann, R. Pustow, and R. Redmer, Icarus **225**, 548 (2013).
[51] R. J. Hemley, H. K. Mao, L. W. Finger, A. P. Jephcoat, R. M. Hazen, and C. S. Zha, Physical Review B **42**, 6458 (1990).

SUPPLEMENTARY TEXT

Sample Preparation and Characterization

Diamond anvil culets diameters of 300 μm flat, or beveled 300 μm with 100 μm culet were used with Re gaskets. Foils were 30-60 μm across with holes of 5-10 μm diameter, and 3-12 μm thick, whereas cavities were at least several μm thicker than the foil in typical experiments. High-purity hydrogen gas was pressure-loaded. In total, 9 sample loadings were made.

Samples were prepared, as in the prior experiment on noble gases [33], by placing metallic couplers containing small holes directly on a diamond culet, prior to pressure-loading of samples. This was done to add stability to coupler position while performing high-temperature experiments, and to ensure the coupler surfaces were orthogonal to the optical axis of the DAC. Interference fringes indicate that the gaps between the coupler and anvil on which it rested was of order a few wavelengths of light at most, so ~1 μm. Laser heating was performed by heating the coupler on the opposite surface (Fig. S1).

Low-pressure experiments (P<60 GPa) were performed with the large culets, and so corresponded to larger sample chambers, with total cavity thicknesses of 10-25 μm, and coupler thicknesses of 6-12 μm. Higher pressure experiments (P>60 GPa) with small culets corresponded to significantly smaller samples of 5-10 μm total thickness and couplers of 3-6 microns in thickness.

Samples were originally configured to permit transient absorption measurement by reflection from foils [33], in addition to transmission, however foil optical changes during heating prevented successful measurements. Specifically, a permanent darkening of the reflective foil, even after a few μs heating, was observed and was attributed to fast interfacial reaction.

Anvils often fractured when subjected to the highest achievable temperatures (4,000 to 6,000 K), which was attributed to rapid hydrogen diffusion into the anvil. Above ~60 GPa hydrogen loss from the sample was reduced and anvil failure eliminated, improving sample stability, though total heating duration remained limited to less than ~1 ms.

DC conductivity model for hydrogen

The phenomenological model fitted to the DC conductivity data (see text) assumed transition temperature and width varied with density ρ as $T_c^* = a_c + b_c\rho$ and $T_w^* = a_w + b_w\rho$, where $\rho(P) = \rho_0 + c\,P^n$ was given as the density on the 300 K isotherm at pressure P [51]. With these assumptions, the best fit parameters, for σ in S/cm, T in K, ρ in mol-H_2/cc, and P in GPa are $\sigma_m^* = 3.41$, $\sigma_j^* = 20.9$, $a_c = 2.22 \times 10^{-4}$, $b_c = 1.41 \times 10^{-3}$, $a_w = 5.25 \times 10^{-4}$, $b_w = -3.86 \times 10^{-4}$, $\rho_0 = 0.0412$, $c = 0.0417$, $n = 0.437$. Note that these fit parameters are based on shock temperature calculations [3,29] that assumed a continuous IMT, which are considered to be consistent with the present direct observations.

We now review the design, physical significance, and phenomenological basis of this model.

(1) During the IMT, it was previously found that $\log(\sigma_0)$ is proportional to $1/T$ [11,12,29]. This model using the *erfc* function has such a linear relationship during the transition, such that in the transformation region it is equivalent to a semiconductor excitation model similar to that used previously for hydrogen during the IMT [3,11,12,29].

(2) The conductivity of hydrogen shows saturation when it becomes fully metallic [3,12-14,16,29]. The *erfc*-function of the model captures this saturation, which cannot be described using only the semiconductor treatment [3,11,12,29]. This model thus describes metallic,

410 semiconducting and insulating (see below) regimes and so includes semiconductor-like behavior
411 only during the transition.
412 (3) The insulating phase in our model fit is found at T<1000 K, conditions where hydrogen is
413 known to be a good insulator in both fluid [15,16,40], and solid [28] phases.
414 (4) Our model implies a density- and temperature- dependent band gap for hydrogen (see below).
415 A gap depending linearly on density only, as used in prior analytical models of the IMT
416 [3,12,29], cannot describe the collected results. However, a linear density dependence of the
417 temperatures of transformation (T_w^*, T_c^*) does provide good consistency between the model and
418 available data.
419 5) The increases in conductivity in our model fit follow closely related changes in optical
420 properties. The onset of visible absorption occurs at $\sigma_0 = 8$ x 10^{-4} S/cm; in the phase diagram,
421 the contour of this conductivity accurately describes absorption onset (solid/bold line in Fig. 1);
422 similarly, a contour of conductivity at 0.65 S/cm (dashed line in Fig. 1) describes accurately the
423 onset of optical reflectivity [14]. Such topological agreement provides good phenomenological
424 support for this model.
425 6) While not occurring in the interpolated pressure range, our model allows for a discontinuous
426 transition (i.e. where transition width $T_w^* \rightarrow 0$). Instead, our model has a weak decrease in T_w^*
427 with pressure in the studied pressure range, consistent with the closing gap between absorption
428 and reflection onset observed with pressure (Fig. 1 and text). Extrapolating to higher pressures,
429 the model suggests $T_w^* \rightarrow 0$ at P>270 GPa (in consideration of fit uncertainty) consistent with
430 dynamic compression observations [16] as well as recent theory [25,27]. The transition
431 temperature ($1/T_c^*$) similarly decreases with pressure, also consistent with optical data and
432 theoretical expectations [5,19-22,25-27].

We now consider in more detail how our DC conductivity model relates to a semiconductor model, as developed previously for the IMT [3,11,12,29]. Within the transformation our model

$$\sigma^* = \sigma_m^* - \sigma_j^*\{-0.5\ \mathrm{erfc}[(T^* - T_c^*)/T_w^*] + 1\}$$

is well described by a linear Taylor expansion about the central transition temperature T_c^*, i.e.

$$\sigma^* = \sigma_m^* - \frac{1}{2}\sigma_j^* + \frac{1}{\sqrt{\pi}}\frac{\sigma_j^* T_c^*}{T_w^*} - \frac{1}{\sqrt{\pi}}\frac{\sigma_j^*}{T_w^*}T^*$$

If we take $\sigma^* = \ln(\sigma_0)$, as opposed to $\log(\sigma_0)$, then the form of this equation is identical to that for conductivity in a semiconductor [3,11,12,29]

$$\sigma^* = \sigma_0^* - \frac{E_g}{2k_B}T^*$$

and thus

$$\sigma_0^* = \sigma_m^* - \frac{1}{2}\sigma_j^* + \frac{1}{\sqrt{\pi}}\frac{\sigma_j^* T_c^*}{T_w^*}$$

and

$$E_g = \frac{2k_B}{\sqrt{\pi}}\frac{\sigma_j^*}{T_w^*}$$

Here fit parameters using $\sigma^* = \ln(\sigma_0)$ become $\sigma_m^* = 7.84$, $\sigma_j^* = 48.1$ (all other model parameters are unchanged). Following this treatment, our model is nearly identical to the semiconductor approach [11,12,29] in the low-pressure limit: at 20 GPa, our model implies E_g = 10.4 eV during the transition (near T_c^*), whereas the earlier semiconductor analysis found 11.7±1.1 eV at these conditions [11,12]. However, a very different behavior is found with increasing pressure, with the band gap remaining large (10.0-12.6 eV at T_c^*) through 140 GPa in our model, rather than closing by this pressure [12,29].

Thus in this model a semiconducting intermediate phase exists between the insulating and metallic states at all studied pressures, in the vicinity of T_c^*, as required by our measurements. Gap closure occurs with increasing pressure at constant temperature (similar to earlier studies), but also with increasing temperature at constant pressure. These features are necessary to fit the current experimental results on hydrogen (this study and Refs. [3,11-14,16,29]) as well as provide general consistency with theory.

Finite Element Modeling

The approach for time-dependent finite-element modeling of temperature in the laser heated diamond cell has been discussed previously [33,39]. The thermochemical parameters used for H_2 are similar to Ref. [39], where heating of hydrogen through the melting transition was modeled. Here we tested possible material models for H_2 with and without an onset of electronic transformation at high temperature. A representative set of finite element model parameters is provided in Table S1. Basic thermochemical parameters were taken from literature tables whereas transport parameters for hydrogen (absorption and thermal conductivity) were varied to obtain the best agreement with the experimental temperature histories. Measured temperature is compared to the maximum temperature in the FE models, located at the coupler surface. Geometrical parameters were chosen based on visual observations and visible interferometry measurements. Two different sample configurations were modeled: a coupler without a hole (e.g. at 30 GPa, Fig. 3) and coupler with a hole (e.g. at 141 GPa, Figs 2, 4, and S2). Our conclusions were not found to be very sensitive to the selected parameterization. To reproduce observed temperature plateaus (Fig. 3), a major increase in absorption (or, alternatively, thermal conductivity) with temperature was required, indicating a high-temperature phase transition to a conductive state.

Table S1. Finite element model parameters for Fig. 3. Parameters for the temperature-dependent absorption model in H_2 are T_C=3300 K and T_0=100 K, with $\alpha_0=10^6$ m^{-1} (with absorption) or α_0=0 m^{-1} (without absorption).

Property/Material	Sample (H_2)	Absorber (Ir)	Anvil (C)
Density (kg/m^3)	420	25220	3500
Thermal Conductivity (W/mK)	100	226	2000
Specific Heat Capacity (J/kg K)	15000	130	509
Surface Emissivity	N/A	.35	N/A
Bulk Absorptivity (1/m)	$\alpha_0\left(1-0.5erfc\left[\frac{T-T_c}{T_0}\right]\right)\times\left(\frac{T-0.8T_C}{0.2T_C}\right)$	N/A	0

Index of refraction of hydrogen

Compared to the imaginary index k (or equivalently, α), which varies by many orders of magnitude in the IMT, the real index n can only vary by, at most, about an order of magnitude, so is always of order 1. Thus to estimate the conductivity of hydrogen during the IMT, we have used n of cold hydrogen at high pressure [44,45], with deviations from this value expected to be small compared with uncertainty. To further examine the validity of this assumption, we have used the Smith-Drude model to compute expected variations in real index as metallization occurs (Fig. S8). This model describes warm dense hydrogen sufficiently well (Fig. 4 and S6) and satisfies the Kramers-Kronig relations, so can accurately treat the relative variations of real and imaginary indices as electronic properties change. This analysis (Fig. S8) suggests the real index should not change by more than a factor of two as the sample becomes absorbing. Melting, which corresponds to no major electronic or density change [28], should also not correspond to

any substantial change in real index. Thus variation in the real index from the ambient temperature values are considered negligible in our experiments, compared to total uncertainty (about an order of magnitude, Fig. 4).

SUPPLEMENTAL FIGURES OVERVIEW

Fig S1 is a schematic summary of our technique [33].

Fig. S2 is a detailed discussion of Fig. 2 in the main text, containing the full data and analysis.

Fig. S3 contains example Raman spectra discussed in the text, including a typical before-and-after spectrum (a), and a spectrum from the single sample where reaction occurred during heating (b).

Fig. S4. shows transient absorption data at several pressures with varying degrees of hydrogen loss.

Fig. S5. is the data compilation [3,11,29,40] and fit used to assess DC conductivity, as in Fig. 1.

Fig. S6 is the theory compilation [17,21,23,24] used to assess the suitability of the Smith-Drude model in describing warm dense hydrogen, as referenced in Fig. 4.

Fig. S7. shows implications of our results for gas giant planets, as discussed in the conclusions.

Fig. S8. considers plausible variations in the real index of refraction of hydrogen as electronic properties change.

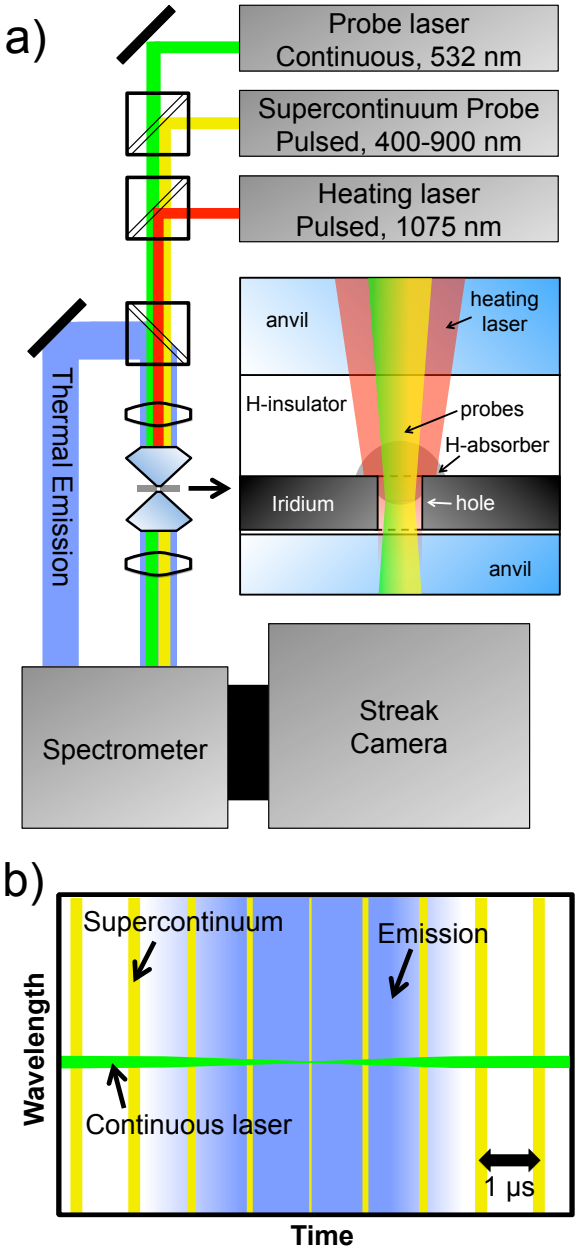

FIG. S1. Schematic of the experiment [33]. (a) Laser heating of a metallic (Ir) foil heats the surrounding, initially-transparent hydrogen. Simultaneously, the sample is probed with a combined beam for transient absorption spectroscopy comprised of a continuous (CW) laser and supercontinuum broadband (BB), which is transmitted through a hole in the foil containing heated hydrogen. Thermal emission is collected through either anvil, and together with probe signal is delivered to a spectrometer with a streak-camera detector; temperatures were measureable from the heated side of the foil for transparent samples or either side for absorbing (emissive) samples. (b) Streak-camera spectrogram of transient absorption during an emissive heat cycle. Laser and supercontinuum probes are discriminated from emission by being monochromatic and pulsed, respectively.

512

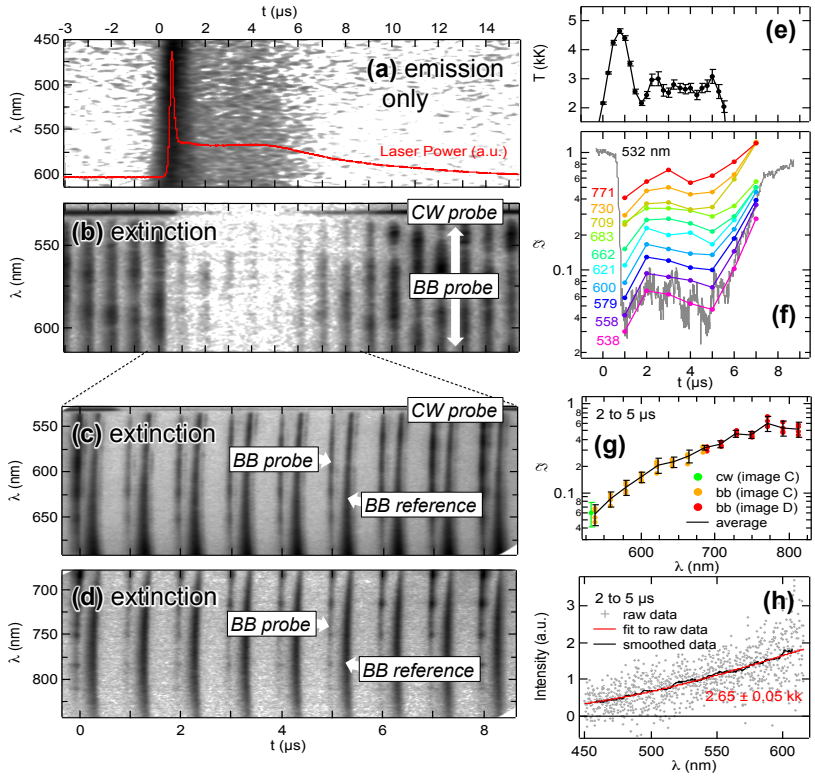

FIG. S2. Detail on Fig. 2. Transient absorption and emission measurements in warm dense hydrogen at 141 GPa and constant laser power. Spectrograms (a-d) are (a) emission alone (20 cycles integrated), (b) Transient absorption (1 cycle) without referencing BB pulses, and (c-d) transient absorption (10 cycles integrated each) with BB pulse references. The latter images are taken using a faster sweep to include a reference pulse at slightly different time delay, appearing immediately after the probe pulse, to track probe spectral instability [33]. A representative temperature history (e) is taken from (a). Transient absorptions (f,g) are taken from (c,d); only the central 7 pairs in (c,d) can be reliably analyzed. Transmission spectra (g) are based on stable temperature zone (e) between 2 and 5 μs. The spectra in two bands (c,d) were combined by assuming agreement at the region of overlap (690 nm) and including systematic offset in systematic error (Fig. 4). The integrated emission from 2-5 μs (h) closely matches a Planck distribution. The temperature between 2 and 5 μs (e) varies in the range 2,400 ± 300 K at this laser power. Temperature errors in (e,h) are fitting error; transmission error in (g) is random uncertainty (1-sigma).

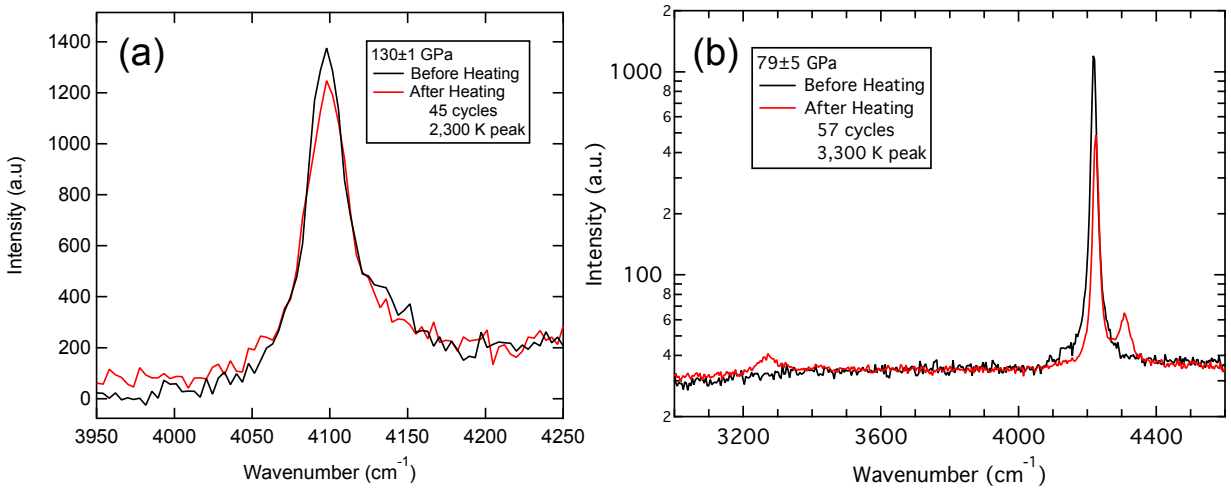

FIG. S3. Raman spectra at (a) 130 GPa (linear scale) and (b) 80 GPa (log scale) before and after heating. The post-heat spectra in (b) contain a hydride signal near 3300 cm^{-1} and related vibron signature near 4300 cm^{-1} as well the pure H_2 vibron (most intense peak, by 1-2 orders of magnitude). Raman evidence of reaction was only seen after the heating series performed in (b); we conclude that bulk reaction was normally prevented by the short timescales of our experiments.

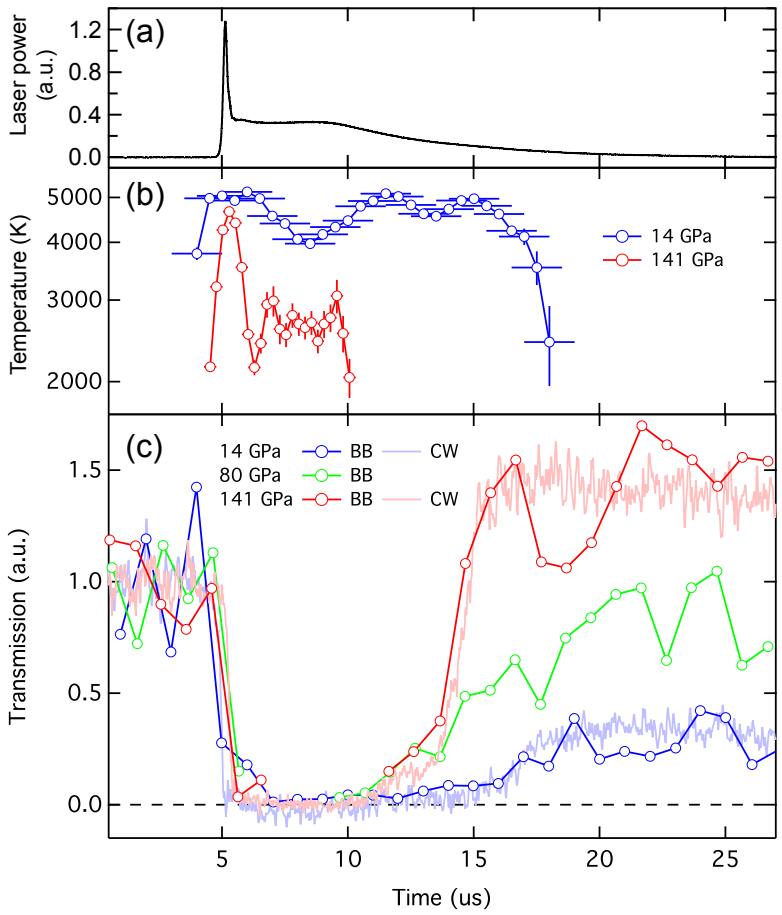

FIG. S4. Transient absorption measurements at 14, 80, and 141 GPa. (a) Laser power. (b) Time resolved temperature, with vertical bars showing temperature fit error and horizontal bars showing time resolution. (c) Transmission behavior during single shots. As a consequence of rapid hydrogen diffusion from the heated area, foil hole diameters often decreased during heat cycles, such that transmission did not always return to the original level. However a high transient extinction due to sample absorption could still be resolved. Slower diffusive loss at higher pressure allowed for relatively stable hole dimensions over many heat cycles. Note that for the 80 GPa experiment, high-time resolution temperature data was not obtained, and sample cavity interference [33] prevented use of the CW probe data. At 14 and 80 GPa, the initial hole size was larger than the probe spot, and closure of the hole was clearly evident visually and in the transmission data; at 141 GPa, the initial hole size was similar in size to the probe spot and remains so after heating. In this experiment, small changes in hole shape during heating (attributed to local melting around the rim of the hole) contributed to a small permanent increase in transmission during heating.

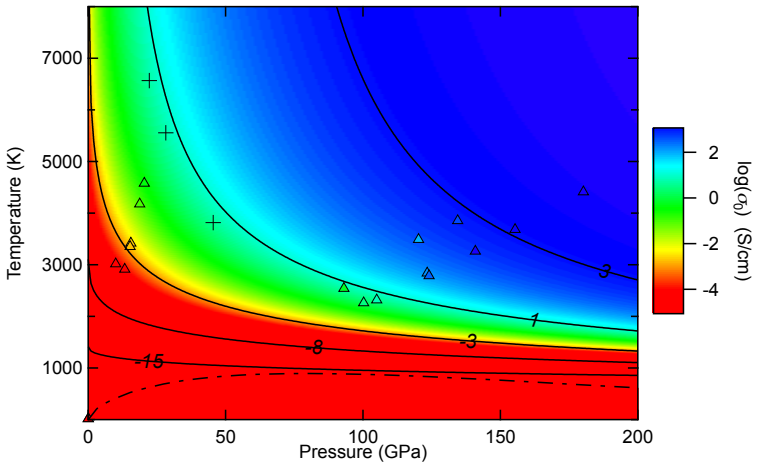

FIG. S5. Detail on DC conductivity model. Dynamic compression [3,11,29] and cryogenic [40] conductivity data on dense hydrogen and deuterium fluid used in our fit are given by colored triangles. The colors (as in Fig. 1) and black solid contours labeled with corresponding conductivity in log units (log (σ_0), in S/cm) are the conductivity model fit. The melt curve is the dashed dotted line [28]. The onset of optical reflectivity in shock compression (crosses) [14] follows the trend of fitted conductivities, with the critical conductivity for reflectivity ~1 S/cm. Pressure and temperature conditions of transformation are similar in deuterium and hydrogen [3,12,14,29], allowing for this global fit; small differences in the phase diagrams are averaged over, as there is good coverage of data for both isotopes in the examined domain.

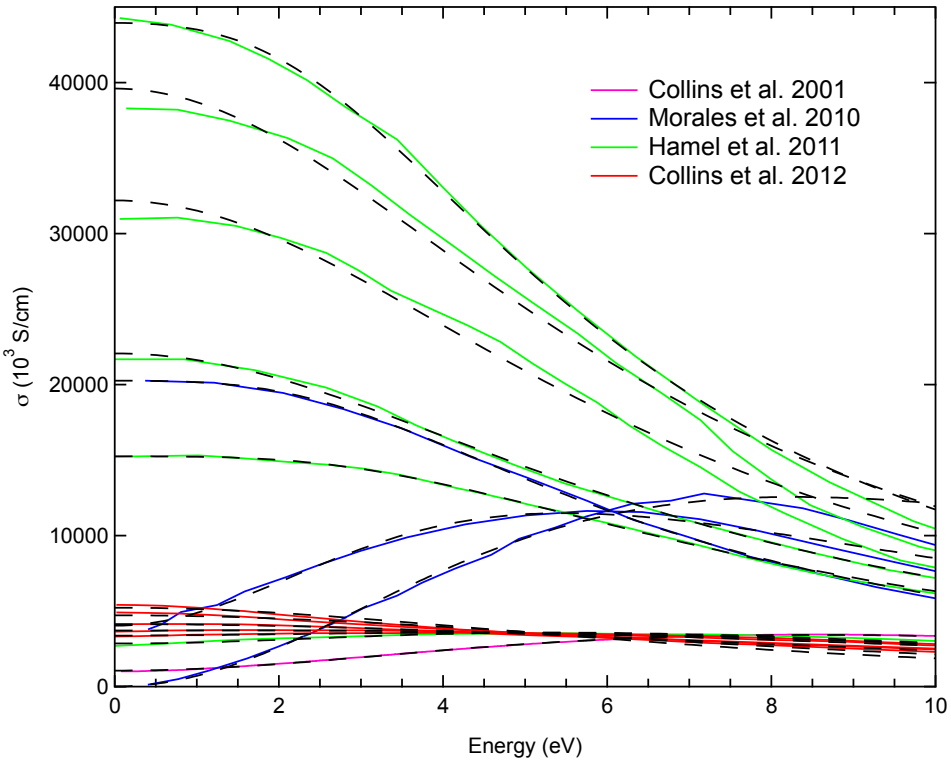

FIG. S6. Detail on Fig. 4. Smith-Drude [46] fits (dashed curves) to conductivity theory for warm dense hydrogen and deuterium at metallization; results are for 24-6000 GPa, 1000-125000K, and 0.3 to 5.4 g/cc [17,21,23,24]. Smith-Drude fits were obtained from the range 0-8 eV. In some cases where spectra had Drude-like character the fit was not fully constrained, in which instances *C* was set to zero for the fit (Drude model).

530

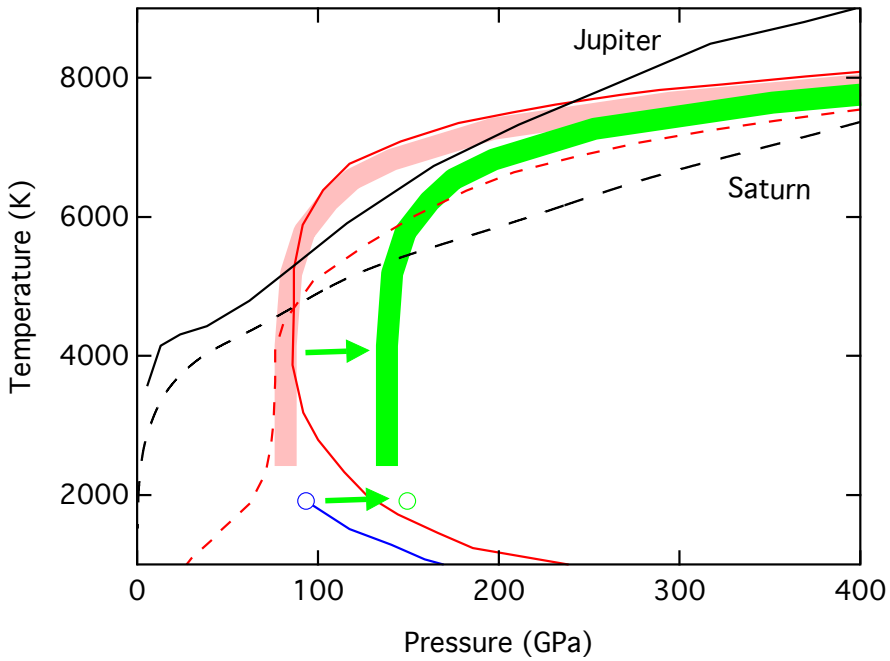

FIG. S7. Effect of high-pressure metallization in hydrogen on phase separation in giant planets. Shown are the predicted maximum temperatures of immiscibility in the hydrogen-helium system (red solid [5] and dashed [47] curves, red band showing upper limit) with corresponding location of the critical point (blue circle) and first-order metallic transition (blue line) [5,47]. Shifting the critical point to higher pressures (green arrow) as required by our measurements to 150 GPa, the upper limit on immiscibility, tied to the first-order metallization [4,5], shifts (green band) to fall outside the conditions of Jupiter's [49] interior (solid black line). Also shown is Saturn's interior [50] (dashed black), where immiscibility conditions remain plausible.

531

532

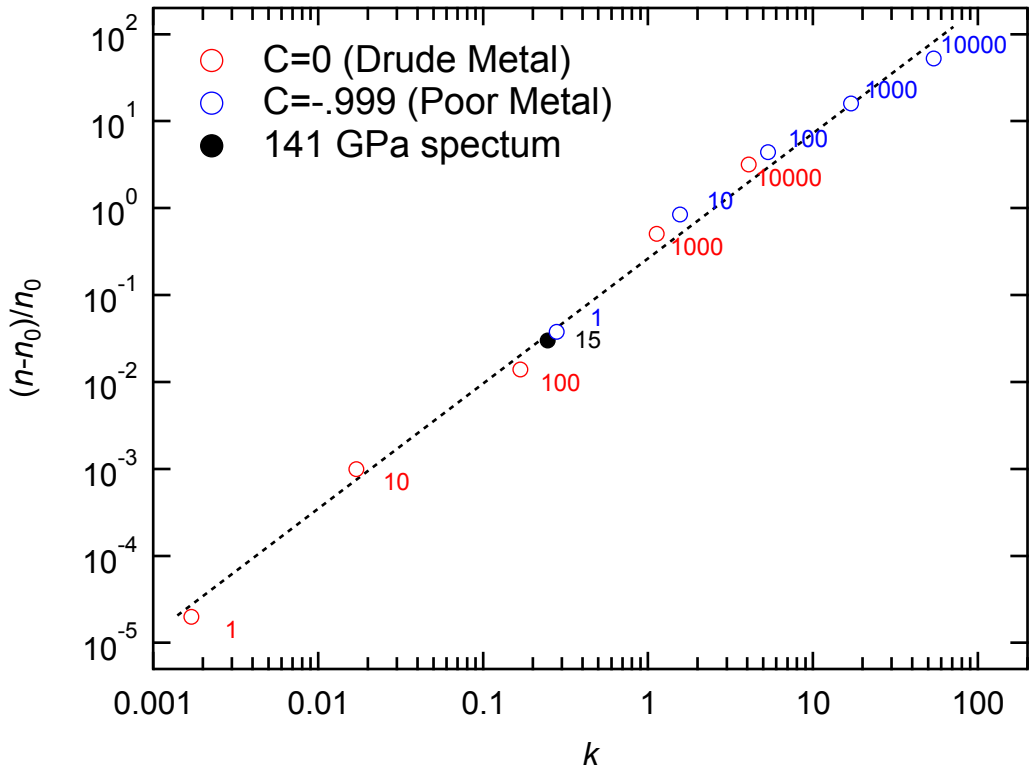

Fig. S8. Effect of metallization on the index of refraction, according to the Smith-Drude model. Results are at optical energy of 2 eV, assuming $\tau = 10^{-16}$ s, a range of σ_0 (values listed in S/cm), and C=0 (red) or C=-0.999 (blue); fit to present data at 141 GPa is the black point. The fractional change in real index n relative to that of the insulating state (n_0) is given as a function of the imaginary index $k = \alpha c/2\omega$. At conditions where k<1 the change in n is less than a factor of two, and it is a few percent at conditions of the 141 GPa measurements (Fig. 4).

533